Multilayer thin film growth on crystalline and quasicrystalline surfaces: A phase-field crystal study

Srevatsan Muralidharan, Raika Khodadad, Ethan Sullivan, and Mikko Haataja

Phys. Rev. B **85**, 245428 — Published 14 June 2012

DOI: 10.1103/PhysRevB.85.245428

Multilayer Thin Film Growth on Crystalline and Quasicrystalline Surfaces: A Phase-field Crystal Study

Srevatsan Muralidharan*
Department of Mechanical and Aerospace Engineering, Princeton University, Princeton, New Jersey 08544

Raika Khodadad and Ethan Sullivan
Princeton Institute for the Science and Technology of Materials (PRISM), Princeton University, Princeton, New Jersey 08544

Mikko Haataja†
Department of Mechanical and Aerospace Engineering, Princeton Institute for the Science and Technology of Materials (PRISM), Program in Applied and Computational Mathematics (PACM), Princeton University, Princeton NJ 08544 and School of Mathematics, Institute for Advanced Study, Princeton NJ 08540

(Dated: June 5, 2012)

In this paper, we explore the effects of misfit strain fields on both heterogeneous nucleation behavior and anisotropic growth of islands at submonolayer coverages and compositional patterning at complete monolayer coverage via simulations of a phase-field crystal model. In particular, deposition on top of a herringbone structure and quasicrystalline (QC) substrate are considered, the former representing a system with spatially periodic misfit strain fields arising from the presence of surface dislocations, while the latter representing a system which inherently possesses a wide range of local, aperiodic misfit patterns. In the case of single component systems, we demonstrate that misfit strain fields lead to heterogeneous nucleation behavior and anisotropic island growth. In the case of QC substrate, a wide range of morphologies, such as coexistence of *locally* hexagonally ordered atomic clusters within a larger scale arrangement with overall QC symmetry and so-called "starfish" aggregates, is observed in pure system at sub-monolayer coverages when the adlayer-substrate interaction strength and lattice mismatch are tuned. In the case of bulk-immiscible binary systems at complete monolayer coverage, strain-stabilized compositional domains emerge at low line tension values for both substrates. Interestingly, the compositional domains on the QC substrate inherit their symmetries at sufficiently low line tension values, while at larger line tension values, the domain structure begins to resemble the classical spinodal microstructure. Such domain structures should be readily observable in colloidal systems in which attractive inter-particle and particle-substrate interactions can be tuned.

PACS numbers: 68.55.A-,68.35.Md,68.35.Dv

I. INTRODUCTION

It is well known that ordered surface nanostructures can be exploited in a wide range of applications, including catalysis[1,2], magnetic storage devices[3], and optical tweezers[4]. The efficiency and functional properties of these systems critically depend on a number of factors, such as typical feature size and polydispersity, local composition, defect structure, and interfacial stresses[1,3]. As the feature size decreases below $\sim$ 100nm, however, standard top-down fabrication methods (such as electron beam lithography) become ineffective[5]. As an alternative, bottom-up approaches involving direct self-assembly driven by misfit strains between different layers during heteroepitaxial growth have rapidly gained popularity[5–7]. Here, the resultant strain relaxation often leads to the formation of ordered surface defect structures, such as herringbone, moire patterns, stripes, and trigons[8–12], which can then be used as templates for further deposition of ordered clusters of atoms or alloys[3,13]. In particular, the effective periodicity of the substrate is transferred "bottom-up" to the subsequent growth layers[5–7].

Recently, a more exotic system, which has been gaining interest as a possible template for self-organized thin film growth, is provided by the surface of a quasicrystal (QC)[14–19]. QCs are structures which possess long-range orientational order but are not periodic, and which thus possess adsorption sites and associated local misfit patterns arranged in an aperiodic manner. This lack of periodicity leads to interesting possibilities for epitaxy involving QC substrates. In this regard, one of the most commonly studied system is the deposition on the five-fold surface of an icosahedral quasicrystal. In particular, the interplay between the local, ordered structure favored by the depositing adatoms and the aperiodic arrangement favored by the QC substrate may give rise to intriguing thin film morphologies.

From a theoretical perspective, a quantitative model to investigate self-assembly in such epitaxial systems must incorporate elastic deformations, misfit strains, formation of defects (such as dislocations and stacking faults), and compositional patterning resulting from any heterogeneous redistribution of constituent atoms in multicomponent systems at nanometer length scales. While some atomistically detailed models are capable of incorporating dislocations and other defects (such as stacking faults), they are largely restricted to modeling one-dimensional single-component or binary systems[20]; extension of such methods to spatially-extended, two component systems, while incorporating defect formation and compositional patterning on an equal footing, is highly non-trivial. Previously, detailed models for compositional patterning assuming pseudomorphic behavior have been developed by Asta, Ozolins and co-workers[21,22], while the effect of substrate defects was phenomenologically incorporated by Yang et al.[23] by introducing an externally applied, symmetry breaking surface potential. Interestingly, Yang et al.[23] demonstrated that such a symmetry breaking external potential indeed can induce the formation of compositional domains within additional layers. A more accurate description of the adatom-substrate interaction, however, is required to investigate the nucleation and growth of islands at submonolayer coverages on substrates with regular dislocation strain patterns[2,13].

To this end, in this work we demonstrate that the phase-field crystal (PFC) model introduced in Ref.[24] for ultrathin films, which overcomes the obstacles discussed above, can be further developed to investigate growth of multi-layer, ordered, self-assembled heteroepitaxial systems. The model is employed to investigate growth of pure and binary systems on substrates which possess a regular arrangement of misfit dislocations and substrates with QC symmetry. First, we demonstrate that the model can quantitatively capture the formation of regular misfit dislocation patterns in the case of Ag deposited on Ru(0001). Then, we turn to a more generic study of single component and binary systems. In particular, we demonstrate that periodic misfit dislocation strain fields control both the nucleation behavior of islands at submonolayer coverages in pure systems and formation of spatially periodic compositional domains in misfitting bulk-immiscible binary systems. In the case of the QC substrate, on the other hand, a wide range of morphologies, such as coexistence of *locally* hexagonally ordered atomic clusters within a larger scale arrangement with overall QC symmetry and so-called "starfish" aggregates, is observed in pure system at submonolayer coverages when the adlayer-substrate interaction strength and lattice mismatch are tuned. Finally, a misfitting binary system deposited on the QC substrate displays compositional patterning with QC symmetry at low compositional line tension values. Such domain structures should be readily observable in colloidal systems in which attractive inter-particle and particle-substrate interactions can be tuned.

The rest of this manuscript is organized as follows. In Sec. II we briefly review the continuum phase-field crystal approach employed in this work, while in Sec. III we first investigate the formation of surface defect patterns in the case of Ag deposited on Ru(0001), and then turn to the nucleation and growth of islands in single-component systems and compositional domain formation in bulk-immiscible binary systems on both regular surfaces with periodic strain patterns and quasicrystalline substrates via numerical simulations. Finally, a brief discussion and concluding remarks can be found in Sec. IV.

II. THEORETICAL APPROACH

Physically, the growth process of a thin film in the layer-by-layer mode can be described in terms of successive growth of individual monolayers on a substrate, whose properties may vary from one layer to another. In order to account for the composition and local morphology of a given layer, we take advantage of the phase-field crystal (PFC) method[25–30], which is especially well-suited for the study of thin film growth[24,31–34]. This methodology can be viewed as a bridge between atomistic simulations and the more traditional phase field approaches[36–38]. Similar to the phase field technique, the system is described by a characteristic free energy functional expressed in terms of one or more continuum fields. In this case, however, the key continuum field is a local time-averaged, smoothly varying single-particle density endowed with the periodicity of a crystal lattice. The PFC approach is closely related to classical density functional theory[28,39], and enables the study of collective phenomena at the atomic length scale over mesoscopic (i.e., diffusive) time scales as driven by a (dynamic) minimization of the free energy.

Following our previous work[24], our starting point is a dimensionless free-energy functional (see Appendix A for the non-dimensionlization procedure) for the i^{th} layer, given by

$$F_i[\rho_i, c_i] = \int \left[\left(\frac{\rho_i}{2} \left(r_i(c_i) + \left(q_i(c_i)^2 + \nabla^2 \right)^2 \right) \rho_i + \frac{\rho_i^4}{4} \right) + V_i(c_i)\rho_i \right.$$
$$\left. + \quad f_0 \left(\frac{w_0^2}{2} (\nabla c_i)^2 - \frac{\theta_c}{2} c_i^2 + \frac{\theta}{2} [(1+c_i)\log(1+c_i) + (1-c_i)\log(1-c_i)] \right) \right] d\mathbf{r}. \tag{1}$$

Here, $\rho_i(\mathbf{r}, t)$ denotes the atomic density field of the i^{th} layer, $c_i(\mathbf{r}, t)$ denotes the concentration field (with fixed spatial average $\bar{c}_i = 0$ or 1 corresponding to 50/50 mixtures or pure systems investigated in this work and $c = \pm 1$ representing different atomic species), $V_i(c_i)$ denotes the species-specific substrate-film interaction energy, $q_i(c_i)$ incorporates the bulk lattice constants of different species (treated as adjustable parameters herein), f_0 controls the relative importance of elastic and chemical energies, θ is related to the dimensionless temperature [cf. Appendix A], θ_c is related to the critical temperature above which there is no phase-separation in the bulk system, $w_0 > 0$ contributes to interfacial energy between different species, and $r_i(c_i)$ is the degree of undercooling. As in our previous work, we will consider binary systems which are immiscible in bulk, and which may form alloys due to substrate interactions. Note that by setting $f_0 = 0$ and $c_i = 1$ in Eq. (1), one can recover the case of deposition of a single-component species on a substrate. Also, note that the functional forms of $V_i(c_i)$ and $q_i(c_i)$ will be specified in the next section.

In order to model the growth dynamics, we assume that the dynamics of the layer that is currently deposited can be described as effectively two-dimensional growth on top of the previously grown monolayer, which acts as a template for further growth. That is, the film is assumed to grow in the so-called Frank-van der Merwe (or layer-by-layer) mode[40], which is often observed in heteroepitaxial systems during early stages of growth. Furthermore, it is assumed that both the substrate and the previously deposited monolayers remain effectively "frozen" such that there is no intermixing between layers or elastic relaxation within the layers[21,41–43]. Intermixing can be neglected when films are grown at sufficiently low temperatures where bulk diffusion does not play any significant role, and elastic relaxation processes associated with either misfit dislocation nucleation above a critical thickness[44] or a morphological transition from the layer-by-layer to 3D island growth mode[40,45] are not relevant for the systems of interest here. Under these assumptions, the dynamics governing the behavior of the local composition (c_i) and morphology (ρ_i) of the newly deposited partial or full monolayer can be described via the following dimensionless, non-linear, stochastic partial differential equations:

$$\frac{\partial \rho_i}{\partial t} = \nabla^2 \left(\frac{\delta F_i}{\delta \rho_i} \right) + \eta_i, \tag{2}$$

where η_i denotes a Gaussian noise term with mean $\langle \eta_i \rangle = 0$ and variance $\langle \eta_i(\mathbf{r}, t)\eta_i(\mathbf{r}', t') \rangle = -2\tilde{T}\nabla^2 \delta(\mathbf{r} - \mathbf{r}')\delta(t - t')$ in accordance with the fluctuation-dissipation theorem, and

$$\frac{\partial c_i}{\partial t} = M_c \nabla^2 \left(\frac{\delta F_i}{\delta c_i} \right). \tag{3}$$

In principle, one should also include stochastic fluctuations in Eq. (3). However, all physical phenomena investigated in this work involving multi-component systems are not associated with homogeneous nucleation processes, and hence the neglect of the noise term is warranted[46]. Finally, in order to eliminate spatial variations in $c_i(\mathbf{r}, t)$ within a single atom, we impose the condition $\hat{c}_i(\mathbf{k}, t) = 0$ for $k^2 > k_f^2$, where k_f denotes a cutoff wave number to be specified below, and $\hat{c}$ denotes the Fourier transform of $c_i(\mathbf{r}, t)$. We also expand the logarithmic free energy in Eq. (1) in powers of c up to c^{52} in order to impose the condition $|c_i(\mathbf{r}, t)| \leq 1$ at all times[24].

III. NUMERICAL SIMULATIONS

We have carried out extensive numerical simulations to investigate nucleation and growth processes of monolayer thin films on both crystalline and quasicrystalline surfaces using the formalism discussed in Section II. We begin the exploration of the model by considering nucleation and growth processes on a regular, crystalline surface. The details of the numerical method can be found in Appendix B. To facilitate visualization of the configurations, we first extract the local maxima from $\rho_i(\mathbf{r}, t)$ and assign equivalent particle positions to these maxima, and then plot the particles; for binary systems, particle identities at maxima are fixed by $c_i > 0\,(< 0)$ representing A (B) atoms.

A. Nucleation and growth on crystalline surface

1. *Formation of herringbone structures*

Our first application of the formalism concerns the growth of a misfitting, monolayer thin film on a metallic surface; as a concrete example, we will consider the case of Ag on Ru(0001) characterized by the primitive lattice vectors $[1\,0\,0]$ and $\frac{1}{2}[1\,\sqrt{3}\,0]$. Experiments have demonstrated that the lattice mismatch between the Ag layer and Ru(0001) layer is accommodated by the formation of a so-called "short-period herringbone" structure (SHB), which is characterized by a regular zig-zag arrangement of edge dislocations[11,12]. These edge dislocations form when stripes of Ag with fcc and hcp stackings, separated by Shockley partial dislocations that run along the different $\frac{1}{2}[1\,\sqrt{3}\,0]$ directions, meet. To model this system, we set $f_0 = 0$ and $c_1 = 1$ in Eq. (1), and employ a simple form for the film-substrate potential, which allows us to conveniently tune the relative interaction energies of an adatom on the substrate hcp, fcc, or bridge sites, respectively[47]: $V_1 = -V_a \sum_{i=1}^{i=3} \cos(\mathbf{K}_j \cdot \mathbf{r}) + V_b \sum_{i=1}^{i=3} \sin(\mathbf{K}_j \cdot \mathbf{r})$, where $\mathbf{K}_j = [\cos(2\pi j/3), \sin(2\pi j/3)]$ (j=1,2,3) denotes the leading reciprocal lattice vectors of the hexagonally ordered surface. As detailed in Ref.[24], choosing $V_a = 4.7 \times 10^{-3}$, $V_b = 0$, $\bar{\rho}_1 = 0.25$, and $r_1 = -0.3$ allows us to match the elastic properties of the adlayer and the film-substrate interaction to those determined from first-principles calculations[48]. Furthermore, we set $K_j = 1$ and $q_1 = 0.9480$ in order to incorporate the +5.5% misfit between the substrate and the adlayer. The grid spacing, simulation box-size and the time stepping used were $\Delta x = \pi/(2\sqrt{3})$, $\Delta y = \pi/4$, $N_x = 512$, $N_y = 512$ and $\Delta t = 0.5$. Other parameters that were employed in the time-stepping algorithm in Eq. (B1) were set to $a_1 = 0.252$, $a_2 = 0.6$, and $a_3 = 0.4$. In order to facilitate the equilibration of the system, we carry out a simulated annealing procedure wherein the noise term is active in the beginning of the simulation, and is subsequently reduced to zero as the simulations proceed.

Several distinct morphologies emerge depending on the initial conditions. Starting from a perfectly misfitting Ag layer on top of the Ru(0001) substrate with a dimensionless temperature $\tilde{T} = 9.1 \times 10^{-3}$, Ag atoms become displaced from their bulk equilibrium positions as guided by the substrate potential, leading to the emergence of regions with local fcc or hcp stackings, separated by Shockley partial dislocations representing a partially ordered SHB pattern. Over time, these structures anneal and become more regular, albeit very slowly. A typical final configuration is shown in Fig. 1 (a). On the other hand, "compressing" the initial Ag layer along the $\frac{1}{2}[1\,\sqrt{3}\,0]$ direction to force a modulated match with the underlying Ru lattice leads to the formation of alternating regions of fcc and hcp stackings in a lamellar pattern ("stripe phase"). Finally, compressing the initial Ag layer along the $[1\,0\,0]$ direction leads to the formation of a regular arrangement of edge dislocations, which constitute a more ordered SHB pattern, as shown in Fig. 1 (b). Interestingly, upon comparing the energies (in meV per Ru atom) for the ordered HB patterns, stripe, and SHB patterns, we obtain the values 1467.57, 1463.28, and 1467.50, respectively; that is, the stripe phase is the energetically favored one.

It should be noted that in experiments, upon deposition of Ag in excess of a complete monolayer, further surface reconstruction ensues and the SHB pattern morphs into the so-called long-range herringbone (LHB) pattern[12]. This reconstruction is a result of large scale collective motion of atoms that is aided by long-range substrate mediated elasticity, as discussed in Ref.[47]. The assumption of a rigid substrate employed in this work thus precludes the study of such LHB structures. However, the focus of the present work is to explore the role of misfit strain patterns generated by the SHB edge dislocations on the templated growth of ordered heterostructures. As will be discussed next, the resulting strain patterns from the SHB dislocations can be accounted for in the deposition of additional monolayers (partial or complete) of either single or binary component systems by employing ρ_1 as the effective substrate potential for the second layer.

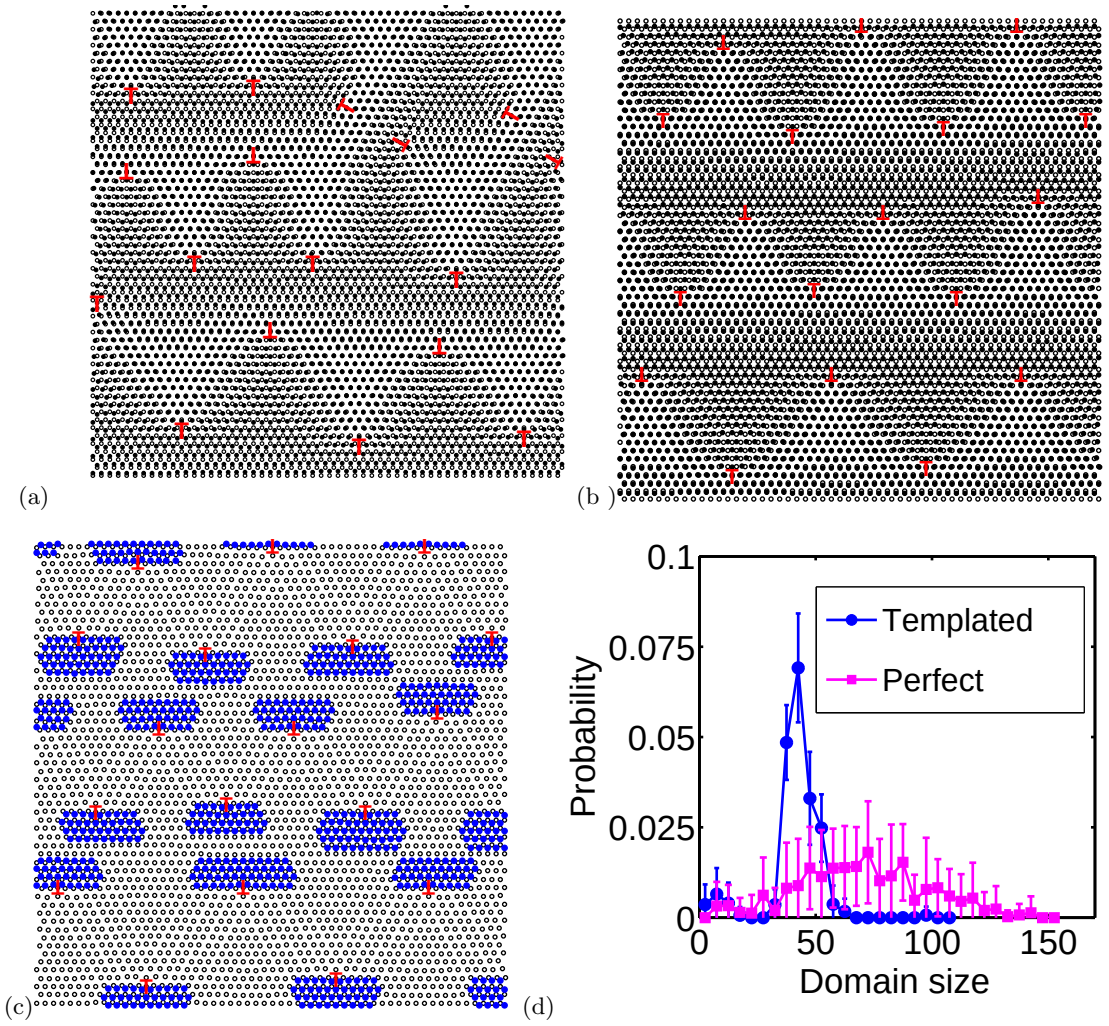

FIG. 1. (Color online) (a) Simulated morphology of ML1 Ag (filled circles) deposited on Ru(0001) substrate. The empty circles indicate the hcp lattice sites of the Ru(0001) surface. Starting from a random initial condition, we observe the formation of a partially ordered arrangement of edge dislocations indicated by red "T" and "inverted T" symbols, representing a partially ordered short-period herringbone (SHB) structure. (b) Starting from an initial condition in which the initial Ag layer is compressed along the $\frac{1}{2}[1\,\sqrt{3}\,0]$ direction, we observe the formation of a regular arrangement of edge dislocations, constituting a more ordered SHB structure. (c) Morphology of a partial monolayer (filled circles) with relative misfit of -5.5% w.r.t to ML1 (empty circles). Note that the nucleation of SML2 commences on top of the edge dislocations within ML1. (d) Island size distribution on templated and pseudomorphic substrates. The size distribution is sharply peaked in the templated substrate case, while it is considerably broader in the pseudomorphic substrate case due to homogeneous nucleation behavior.

2. *Templated growth of single component systems on herringbone structure*

We next study the case of a submonolayer (SML2) of a single component system deposited on top of the templated substrate with ordered SHB structure using Eq. (1) with $V_2 = V_{12}(\rho_1(\mathbf{r}) - \bar{\rho}_1)/2A_1$. Here, A_1 denotes the density amplitude of ML1, which can be approximated by $A_1 = \bar{\rho}_1/5 + \sqrt{-15r_1 - 36\bar{\rho}_1^2}/15$[25,26], while V_{12} denotes the coupling strength between SML2 and ML1. The simulations are started from a supersaturated uniform phase with $\rho_2(\mathbf{r}, 0) = \bar{\rho}_2$, where $\bar{\rho}_2$ is varied to control the fraction of the crystalline phase for SML2 (i.e., the coverage)[25]. More specifically, herein we set $\bar{\rho}_2 = 0.64$, which corresponds to a coverage of 0.23. In addition, we assume that SML2 has a relative misfit of -5.5% w.r.t ML1, i.e., SML2 has the same lattice spacing as that of the original substrate beneath ML1. The rest of the parameters are set to $r_2 = -0.75$, $V_{12} = 0.3$, $\tilde{T} = 8 \times 10^{-4}$, and $q_2 = 1.058$. The grid spacing, simulation box-size and time step employed were $\Delta x = \pi/(2\sqrt{3})/1.055$, $\Delta y = \pi/4/1.055$, $N_x = 512$, $N_y = 512$ and $\Delta t = 0.5$. Note that the Δx and Δy values used in these particular simulations, in effect, rescale the wave number of ML1 obtained in the previous section to 1. Other parameters that were employed in the time-stepping algorithm in

Eq. (B1) were set to $a_1 = 0.2$, $a_2 = 0.6$, and $a_3 = 0.4$.

Typical morphologies obtained from simulations are shown in Fig. 1 (c). It can be seen that the nucleation of SML2 islands commences on top of the edge dislocations of ML1 as guided by the local elastic strain fields. More specifically, due to the smaller lattice spacing of SML2, the islands initially form on the compressive parts of the misfit dislocations. One can further notice that the heterostructures comprising the SML2 are faceted. Such faceting behavior can be correlated with the inherent anisotropies associated with solid-liquid interface at high undercooling (r) as investigated very recently by Granasy and co-workers[33,49].

In order to quantify the role of the misfit strain fields in the heterogeneous nucleation behavior of SML2, we have carried out a total of 50 independent simulations in order to extract the island size distribution at fixed coverage. The data is shown in Fig. 1 (d). It can be seen that the island size distribution is sharply peaked corresponding to the templated substrate in comparison with a perfectly pseudomorphic substrate, for which the nucleation behavior is homogeneous, leading to considerably broader size distribution. Furthermore, upon increasing the coverage of SML2, the islands grow in a highly anisotropic manner as guided by the dislocation strain fields; that is, the dislocations give rise to local barriers for domain growth and thus constrain further island growth. It should be noted that while experiments[13] indicate that the heterogenous nucleation of islands on top of herringbone pattern proceeds first via site specific exchange processes with the underlying substrate not included in the present approach, the presence of misfit strain fields alone is sufficient to guide the nucleation and patterning of such islands.

3. Compositional domain formation in bulk-immiscible binary alloy systems on herringbone structure

Next, we consider the case of a complete monolayer deposition of a two component, bulk-immiscible system on top of the herringbone structure of ML1. The ML1-ML2 interaction potential is incorporated by setting $V_2(c) = V_{12}(c)(\rho_1(\mathbf{r}) - \bar{\rho}_1)/2A_1$; for simplicity, we will consider only the case for which $V_{12}(c) = 0.06$ is independent of composition. Furthermore, as in our previous work[24], we set $r_2(c) = A_r + B_r c$ and $q_2(c) = 1 - \epsilon c/2 + \epsilon^2 c^2/4$, which allows us to independently tune the elastic properties and bulk lattice constants of the corresponding pure systems. More specifically, we set $A_r = -0.75$, $B_r = 0$, $\theta_c = 3$, $\theta = 1.5$, and $w_0 = 2\pi/\sqrt{3}$. A value of $\epsilon = 0.11$ is chosen for the misfit, implying that the $c = -1$ component has the same lattice spacing as the original substrate. The grid spacing and simulation box-size used were $\Delta x = \pi/(2\sqrt{3})/1.055$, $\Delta y = \pi/4/1.055$, $N_x = 512$, $N_y = 512$. The time stepping used was $\Delta t = 0.4$ for $f_0 < 0.0352$ and $\Delta t = 0.2$ for $f_0 > 0.0352$. Other parameters that were employed in the time-stepping algorithm in Eqs. (B1) and (B14) were set to $k_f = 0.59$, $a_1 = 0.2$, $a_2 = 0.55$, and $a_3 = 0.45$. The simulations are started with random initial conditions for both c and ρ_2 with $\bar{c} = 0$ and $\bar{\rho}_2 = 0.35$, and the evolution equations [Eqs. (2) and (3)] are numerically integrated in time in the absence of stochastic fluctuations.

Final equilibrated domain morphologies on the templated substrate are displayed in Figs. 2 (a) and (b) for compositional domain wall line tension values $f_0 = 3.7 \times 10^{-3}$ and 27.8×10^{-3}, respectively. It can be seen that the morphology in both cases is characterized by spatially periodic compositional domains, stabilized by the dislocation strain fields. In particular, tensile regions of ML1 attract the $c = -1$ species, while the $c = +1$ species accommodates the spatial preference of the other species by occupying the compressive regions along the substrate. Furthermore, Fig. 2 (c) shows the corresponding morphology of ML2 when deposited on top of a perfectly commensurate surface layer with line tension value $f_0 = 27.8 \times 10^{-3}$. It is noteworthy that in the latter case, line tension is strong enough to drive the system towards complete phase separation. In the herringbone case, the presence of the elastic strain field is sufficient to counteract line tension forces, leading to compositional patterning. In this regime, we find that the domain length scales are set by the dislocation spacing and the sizes of the strain-stabilized domains display only a gradual variation with line tension.

To better quantify the templated compositional domain formation process, we have extracted the typical domain size L_c from $L_c \equiv L^2/L_{int}$ (in units of the substrate lattice spacing), where L^2 is the total area of our simulation cell and L_{int} denotes the total interface length between the compositional domains[24]. To this end, the data shown in Fig. 2 (d) displays the variation of L_c as a function of f_0 for domain evolution on both the templated and the perfectly commensurate surfaces. It can be seen that while L_c is a monotonically increasing function of f_0 with a divergence at a critical value $f_0^* \approx 5.5 \times 10^{-3}$ in the case of the perfectly commensurate ML1, it is characterized by a rather weak f_0 dependence leading up to a divergence around $f_0^* \approx 45 \times 10^{-3}$ in the herringbone case. Interestingly, L_c displays a non-monotonic dependence on line tension for $f_0 \lesssim 37 \times 10^{-3}$ within the accuracy of our data. Within this regime, increasing f_0 leads to an overall "flattening" of the compositional interfaces, as expected. Intriguingly, we occasionally observe specific domain "cleavage" events, in which a connected compositional domain splits into multiple domains. Both processes contribute to the variation of L_c in ways which do not lend themselves to a simple quantitative explanation. Finally, we have explicitly verified that these observations and data hold even when thermal fluctuations with magnitudes up to $\tilde{T} = 1 \times 10^{-3}$ are included in the evolution equations for both ρ and c for several f_0 values, namely $f_0 = 9.3 \times 10^{-3}$, 1.85×10^{-2}, 2.2×10^{-2}, and 2.78×10^{-2}.

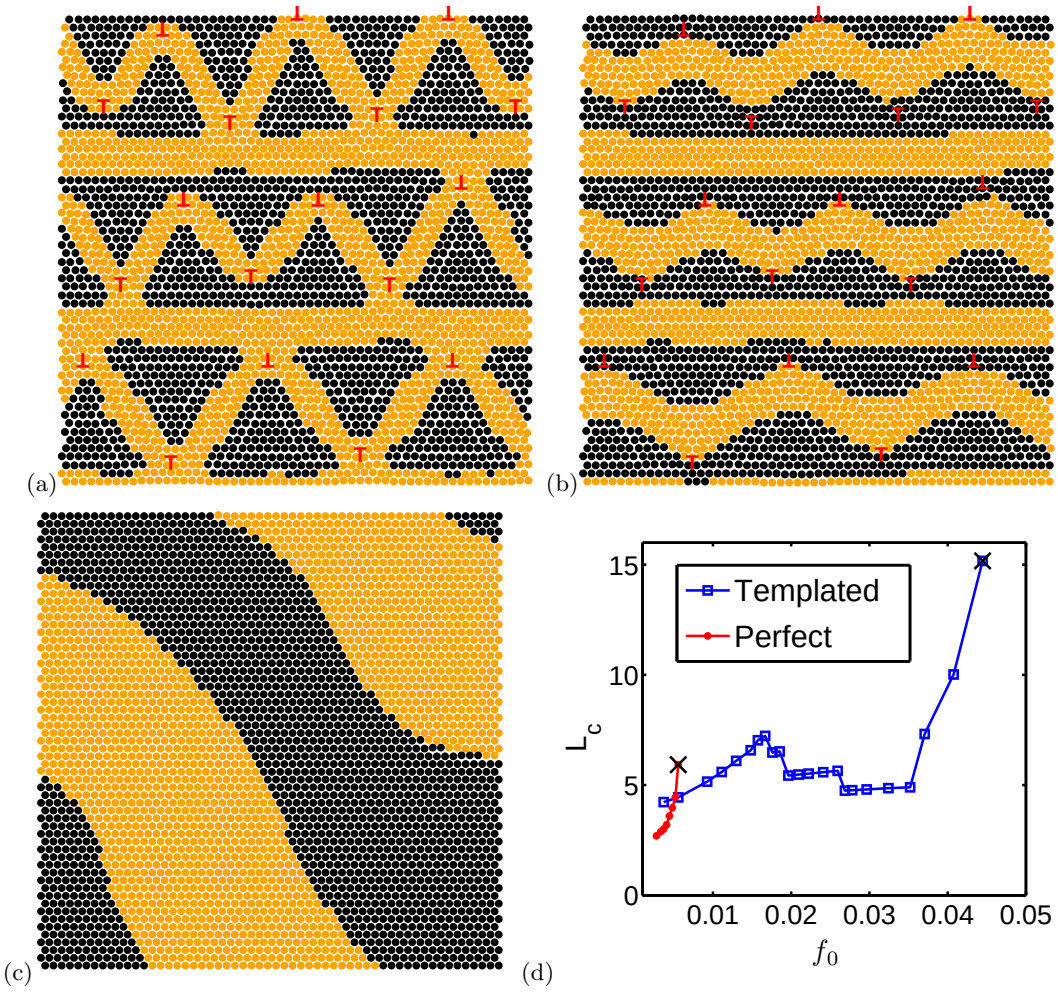

FIG. 2. (Color online) Compositional domain formation on templated and pseudomorphic substrates. (a) and (b) display the equilibrated, strain-stabilized compositional domains obtained with a line tension value of $f_0 = 3.7\times10^{-3}$ and $f_0 = 27.8\times10^{-3}$, respectively, for growth on a templated surface, while (c) displays a coarsened compositional microstructure for growth on pseudomorphic substrate for $f_0 = 27.8\times10^{-3}$. (d) Compositional domain size vs. line tension f_0. It can be seen that while L_c is a monotonically increasing function of f_0 with a divergence at a critical value $f_0^* \approx 5.5\times10^{-3}$ in the case of the perfectly commensurate ML1, it is characterized by a rather weak f_0 dependence leading up to a divergence around $f_0^* \approx 45\times10^{-3}$ in the herringbone case.

B. Nucleation, growth, and compositional patterning on quasicrystalline substrates

Having established the critical role that periodic misfit strain fields play in both promoting heterogeneous nucleation and anisotropic growth of islands at submonolayer coverages and compositional patterning at complete monolayer coverage, we now turn to a discussion of nucleation behavior and compositional patterning on a quasicrystalline (QC) surface. Apart from atomic deposition on a physical adsorbate, one can realize such congruent experimental systems by means of laser interference of colloidal systems[50,51]. As mentioned earlier, one of the most commonly studied epitaxial system involving QCs is the case of deposition on five-fold surfaces of icosahedral QCs. A phenomenological adlayer-substrate interaction potential, which incorporates the proper symmetries, has been very recently proposed by Rottler and co-workers[34]: $V_{QC} = V_0|\sum_{j=1}^{5}\exp\left(i\alpha\mathbf{K}_j\cdot\mathbf{r}\right)|^2$, where $\mathbf{K}_j = [\cos(2\pi j/5),\sin(2\pi j/5)]$. The structure factor of this 5-fold substrate potential is 10-fold symmetric, with the fundamental peaks in the structure factor occurring at wavenumbers $k_1 = \sqrt{2}\alpha[1-\cos(2\pi/5)]^{1/2}$ and $k_2 = \sqrt{2}\alpha[1-\cos(4\pi/5)]^{1/2}$, such that the ratio $k_2/k_1 = (\sqrt{5}+1)/2$ corresponds to the so-called "golden mean". The parameter α is employed to tune the first and second fundamental length scales ($\sim 1/k_1$ and $\sim 1/k_2$, respectively) corresponding to the QC substrate relative to the bulk lattice constant of the adlayer. Below, we employ this adlayer-substrate potential to investigate both single component systems at

sub-monolayer coverages and binary systems at complete monolayer coverage on such surfaces.

1. Island nucleation on quasicrystalline substrate

We first study the role played by the adlayer-substrate interaction strength, V_0, on the morphology of single-component islands at submonolayer coverages. To this end, we set $f_0 = 0$, $c = 1$, $\bar{\rho} = 0.58$, $r = -0.9$, $\epsilon = 0.0$, $\eta = 0.0$, and $\alpha = 0.84$ in Eq. (1). This particular choice of α (implying that $k_1 \approx 1$) was chosen to ensure a good overall match between the first fundamental length scale of the QC substrate and the bulk lattice constant of the depositing particles. Furthermore, the grid spacing, simulation box-size and the time stepping used were $\Delta x = \pi/(2\sqrt{3})$, $\Delta y = \pi/(2\sqrt{3})$, $N_x = 1024$, $N_y = 1024$, and $\Delta t = 0.1$, respectively. Other parameters that were employed in the time-stepping algorithm in Eq. (B1) were set to $a_1 = 0$, $a_2 = 0$, and $a_3 = 0$.

Upon starting from a random initial condition corresponding to a supercooled liquid phase, islands nucleate and begin to grow at sufficiently large adlayer-substrate interaction strengths. Typical equilibrated configurations are shown in Fig. 3 (a) through (c) corresponding to three different V_0 values, namely 9.15×10^{-4}, 9.25×10^{-4}, and 9.45×10^{-4}, respectively. Interestingly, for this range of V_0 values, it can be seen that while the islands retain *local* hexagonal ordering, at sufficiently large scales they conform to the symmetries of the underlying QC substrate. To quantify this competition between short-range and long-range ordering, we have extracted the adlayer structure factor corresponding to $V_0 = 9.15 \times 10^{-4}$ and averaged it over 40 independent simulations. The data is shown in Fig. 3 (d). It can be seen that the structure factor has a dominant "ring" of peaks at $q = 1$, reflecting the local hexagonal ordering of these clusters at different orientations, with additional ten-fold symmetric peaks at smaller wavenumbers, reflecting the emergence of QC symmetries at large scales. Increasing V_0 shifts these ten-fold symmetric peaks towards $q = 1$ (data not shown), as both the hexagonal cluster size and cluster separation decrease. Finally, upon increasing V_0 beyond 1.1×10^{-3}, the QC peaks merge with the $q = 1$ ring. Beyond this point, local hexagonal ordering disappears completely, and the adlayer exhibits only a quasicrystalline symmetry.

A better understanding of island growth kinetics can be obtained by examining island morphologies during the growth phase. To this end, Fig. 4 displays four configurations during the growth of a particular island. In particular, it can be seen that, initially, a seed particle attaches to the center of a 10-fold symmetric substrate adsorption site. Then, an annulus consisting of 7 particles coalesces around the seed particle. Finally, subsequent growth occurs via addition of particles arranged with hexagonal symmetry along the periphery of the cluster, leading to the formation of a defected hexagonal grain, with the core of an edge dislocation residing at the initial nucleation site.

In order to better quantify the nucleation behavior, we have extracted the island size distributions for three different values of V_0. The data is shown in Fig. 5. At the largest V_0 value, the size distribution is unimodal and sharply peaked, while at the smallest of the V_0 values employed, it is also unimodal but significantly broader. On the other hand, the size distribution corresponding to the intermediate V_0 value displays a bimodal form with rather narrow support. In this case, in the simulations it is observed that the larger domains (corresponding to the second peak in the size distribution) nucleate first and form locally arranged "rings" consisting of 10 islands, before a ring of smaller islands (first peak in the size distribution) nucleates and grows.

Finally, we have investigated the effect of the relative misfit between the adlayer and the QC substrate on the morphology of the sub-monolayer film. To this end, we have set $V_0 = 9.15 \times 10^{-4}$ and varied the parameter α. Configurations corresponding to $\alpha = 0.48$ and 0.51 are shown in Fig. 6 (a) and (b), respectively. In the former case, when the adlayer lattice constant is mismatched relative to either of the fundamental length scales of the QC substrate, exotic island morphologies emerge. In the latter case, on the other hand, when the adlayer lattice constant is matched to the second fundamental length scale ($\sim 1/k_2$) of the QC substrate, the particles tend to populate the 5-fold symmetric lattice sites, leading to emergence of so-called "starfish" patterns, which have been observed in quasicrystalline epitaxial systems such as Al/Al-Cu-Fe[19] and Pb/Al-Pd-Mn[35]. Close-up of a starfish island illustrating the local particle arrangements is shown in turn in Fig. 6 (c).

2. Compositional domain formation in bulk-immiscible binary alloy systems on quasicrystalline substrate

Finally, we turn to the case of a full monolayer of a binary system deposited on a QC substrate. Recall that in the case of deposition on the herringbone substrate, we observed the emergence of strain-stabilized compositional domains. Herein, we investigate the possibility of replicating such an effect for deposition on a QC substrate, which inherently presents a much broader range of local misfit patterns. To this end, we chose the following parameters: $\bar{\rho} = 0.35$, $\bar{c} = 0$, $V_0 = 7 \times 10^{-3}$, $r = -0.75$, $\epsilon = 0.2$, $\theta_c = 3$, $\theta = 1.5$, and $\alpha = 0.77$. These particular choices for ϵ and α imply that the lattice spacing of the $c = +1$ component matches well with the first fundamental QC length scale, while the $c = -1$ component has a considerably poorer match with the substrate. In these simulations, the grid

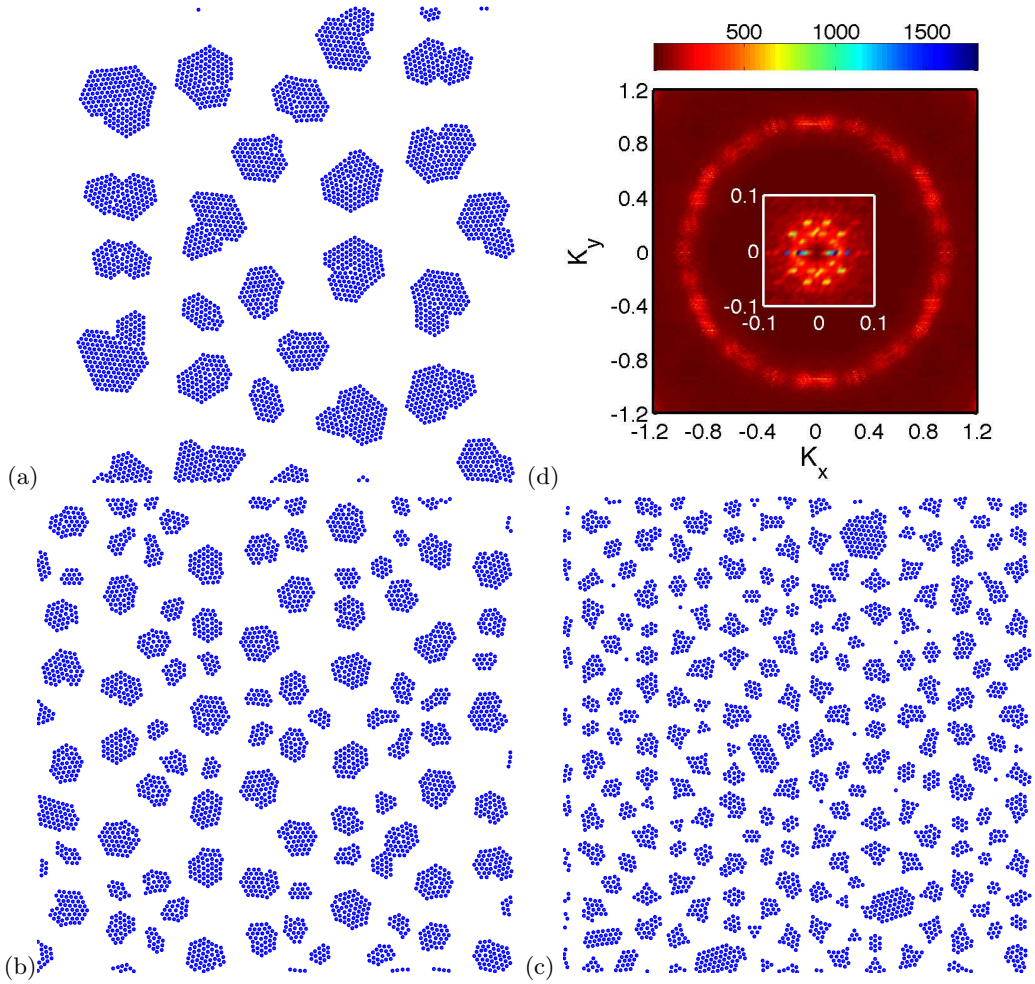

FIG. 3. (Color online) Nucleation of islands and island morphology on quasicrystalline substrate for varying adlayer-substrate interaction strengths V_0 for the case where the adlayer lattice constant is matched to the first fundamental length scale ($\sim 1/k_1$) of the QC substrate. (a) $V_0 = 9.15 \times 10^{-4}$ (b) $V_0 = 9.25 \times 10^{-4}$ (c) $V_0 = 9.45 \times 10^{-4}$. (d) Structure factor corresponding to configuration in (a). It can be seen that the structure factor has a dominant "ring" of peaks at $K = 1$, reflecting the local hexagonal ordering of these clusters at different orientations, with additional ten-fold symmetric peaks at smaller wavenumbers, reflecting the emergence of QC symmetries at large scales. Increasing V_0 shifts these ten-fold symmetric peaks towards $K = 1$, as both the hexagonal cluster size and cluster separation decrease.

spacing, simulation box-size and time-stepping used were $\Delta x = \pi/(2\sqrt{3})$, $\Delta y = \pi/(2\sqrt{3})$, $N_x = 512$, $N_y = 512$, and $\Delta t = 0.3$. Other parameters that were employed in the time-stepping algorithm in Eqs. (B1) and (B14) were set to $k_f = 0.48$, $a_1 = 0.2$, $a_2 = 0.55$, and $a_3 = 0.45$.

Starting from random initial conditions for both ρ and c, typical equilibrated configurations which emerge are shown in Fig. 7 (a) through (c) corresponding to three different line tension values. In all three cases, formation of strain-stabilized compositional domains is observed, with larger values of the line tension corresponding to larger domains, as expected. To better quantify the emerging domain structure, we have again computed the structure factors corresponding to the local composition $c(\mathbf{r})$. The data is shown in Fig. 7 (d) through (f). It can be seen that at low line tensions, the structure factors show well-defined peaks that are ten-fold symmetric, reflecting the formation of compositional domains with QC symmetry. Furthermore, the compositional domains corresponding to the $c = +1$ particles localize at the ten-fold symmetric adsorption sites of the substrate potential, with a center particle surrounded by an annulus of 7 additional particles. This is perhaps not so surprising, as precisely such arrangements of particles were observed during the island nucleation and sub-monolayer growth phase in the corresponding $c = +1$ single component system [cf. Fig. 4 (b)]. At larger line tension values, the domain structure begins to resemble the characteristic of the classical spinodal microstructure, which is reflected in the structure factor by virtue of the ten-fold

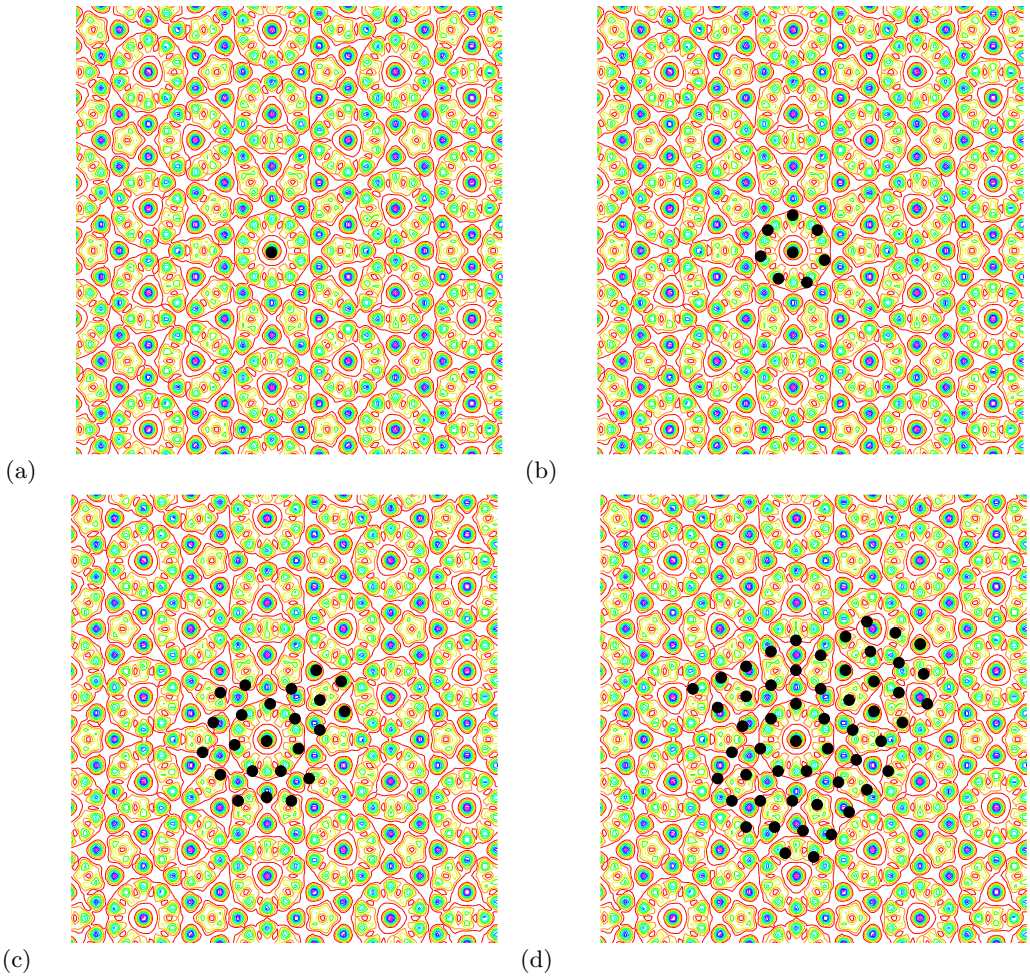

FIG. 4. (Color online) Detailed growth kinetics of a nucleated island on QC substrate for the case where the adlayer lattice constant is matched to the first fundamental length scale ($\sim 1/k_1$) of the QC substrate. Particles are shown in solid black circles, while the contours represent local substrate potential values. (a) Initially, a seed particle attaches to the center of a 10-fold symmetric substrate adsorption site. (b) Then, an annulus consisting of 7 particles coalesces around the seed particle. (c)-(d): Subsequent growth occurs via addition of particles arranged with hexagonal symmetry along the periphery of the cluster, leading to the formation of a defected hexagonal grain, with the core of an edge dislocation residing at the initial nucleation site.

symmetric peaks coalescing into a "ring" around the characteristic wavenumber of the spinodal microstructure.

IV. DISCUSSION

In this paper, we have explored the effects of misfit strain fields on both heterogeneous nucleation behavior and anisotropic growth of islands at submonolayer coverages and compositional domain formation in bulk-immiscible systems at complete monolayer coverage. In particular, deposition on top of a herringbone structure and quasicrystalline (QC) substrate were considered, the former representing a system with spatially periodic misfit strain fields arising from the presence of a regular dislocation network, while the latter representing a system which inherently possesses a wide range of local, aperiodic misfit patterns. This study was facilitated by extensive numerical simulations of a phase-field crystal (PFC) model presented in Sec. II.

First, it was demonstrated that our PFC approach naturally reproduces experimentally observed herringbone patterns in the case of Ag on Ru(0001). Then, the simulated herringbone structure was employed as a substrate for further deposition of generic single component and bulk-immiscible binary systems. In the case of a single-component system deposited at submonolayer coverages, it was shown that misfit dislocations act as heterogeneous nucleation

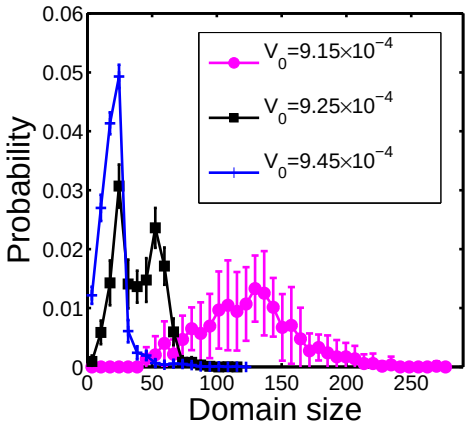

FIG. 5. (Color online) Island size distribution on quasicrystalline substrate at several adlayer-substrate interaction strengths. At the largest V_0 value, the size distribution is unimodal and sharply peaked, while at the smallest of the V_0 values employed, it is also unimodal but significantly broader. On the other hand, the size distribution corresponding to the intermediate interaction value displays a bimodal form with rather narrow support.

sites, and that their elastic strain fields effectively guide the further growth of islands. In the case of binary systems at complete monolayer coverage, we observed the emergence of strain-stabilized compositional nanoscale domains. The characteristic domain length scale is set by the periodicity of the strain pattern with weak dependence on the compositional domain wall line tension up to a threshold value, beyond which coarsening takes place.

In the case of the QC substrate, it was first shown that with appropriately tuned particle-substrate interaction values and adlayer lattice constant matched to the first fundamental QC length scale, islands which nucleate and grow at submonolayer coverages retain *local* hexagonal ordering, leading to defected grains with edge dislocations residing at the initial nucleation sites. However, at sufficiently large scales, the islands conform to the symmetries of the underlying QC substrate. This competition between local and global ordering was quantified in terms of structure factors, and such morphologies should be readily observable in colloidal systems[50,51] in which attractive inter-particle and particle-substrate interactions can be tuned. Interestingly, when the adlayer lattice constant is matched to the second fundamental length scale of the QC substrate, emergence of "starfish" islands were observed. Taken together, these results suggest that a broad range of morphologies can be generated by appropriately tuning the lattice mismatch between the adlayer and QC substrate and the adlayer-substrate interaction potential.

In the case of a binary system deposited on the QC substrate at complete monolayer coverage, it was shown again that compositional domains emerge as guided by the aperiodic misfit strain fields. In particular, the compositional domains inherit the QC symmetries of the underlying substrate at sufficiently low line tension values, while at larger line tension values, the domain structure begins to resemble the classical spinodal microstructure. These morphologies should also be readily observable in colloidal systems.

The work described in this paper can be extended in several ways. First, it would be interesting to allow for intermixing between the deposited layers and elastic relaxation within layers during growth and annealing. This can be done by carrying out full three-dimensional simulations of appropriately constructed, quantitative PFC models; see, e.g., Refs.[31,32] for examples of PFC modeling of 3D thin film growth. Second, incorporating elastic relaxation processes within the substrate would facilitate simulation studies of the formation of long-ranged herringbone structures and subsequent templated growth on such substrates. In principle, this can be achieved by describing the substrate in terms of its own PFC model. However, it would be more computationally efficient to integrate out the elastic deformations within the substrate and incorporate their effect within a 3D PFC description of the thin film. We are currently exploring such approaches. Finally, it would be interesting to incorporate more detailed, atomically-informed adlayer-substrate potentials for the case of deposition on metallic QC substrates. All of the aforementioned extensions would provide critical insights into the nonlinear self-assembly and growth processes on surfaces.

Acknowledgements – Partial financial support for this work was provided by the Princeton Center for Complex Materials (PCCM), a U.S. National Science Foundation Materials Research Science and Engineering Center (Grant DMR-0819860), and by the PCCM REU and RET programs. The authors would like to thank Dr. J. Rottler for useful discussions.

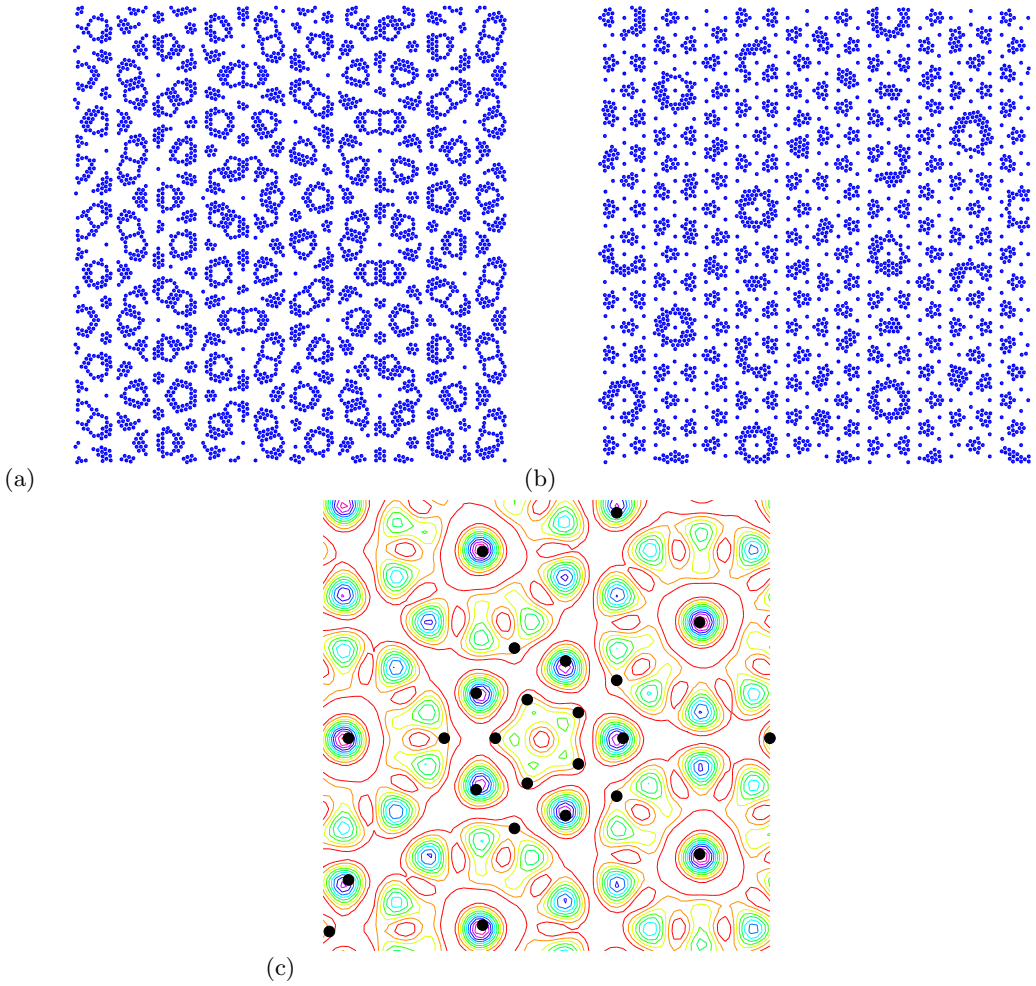

FIG. 6. (Color online) Morphology of sub-monolayer film on QC substrate at different misfits. (a) When the adlayer lattice constant is mismatched relative to either of the fundamental length scales of the QC substrate, exotic island morphologies emerge. (b) On the other hand, when the adlayer lattice constant is matched to the second fundamental length scale of the QC substrate, the particles tend to populate the 5-fold symmetric lattice sites, leading to emergence of so-called "starfish" patterns. (c) Close-up of one starfish island from panel (b). Particles are shown in solid black circles, while the contours represent local substrate potential values.

Appendix A: Non dimensionalization

For completeness, the non-dimensionalization procedure for the system free energy and dynamical equations is presented here. Our starting point is the full dimensional form of the free energy functional, given by

$$\hat{F}_i[\hat{\rho}_i, c_i] = \int \left[\left(\frac{\hat{\rho}_i}{2} \left(\hat{r}_i(c_i) + \lambda \left(\hat{q}_i(c_i)^2 + \hat{\nabla}^2 \right)^2 \right) \hat{\rho}_i + u \frac{\hat{\rho}_i^4}{4} \right) + \hat{V}_i(c_i)\hat{\rho}_i + \hat{f}_0 \left(\frac{\hat{w}_0^2}{2} (\hat{\nabla} c_i)^2 \right.\right.$$
$$\left.\left. - \frac{k_B T_c}{2} c_i^2 + \frac{k_B T}{2} [(1+c_i)\log(1+c_i) + (1-c_i)\log(1-c_i)] \right) \right] d\hat{\mathbf{r}}. \tag{A1}$$

As discussed in detail by Elder and co-workers[26,28], the parameters $\hat{r}_i$, λ, $\hat{q}_i$, and u can be related to the liquid state structure factor and elastic constants of the hexagonal crystal, while the terms involving the composition account for the bulk and interfacial thermodynamics of the binary system. Finally, the term $\hat{V}_i(c_i)\hat{\rho}_i$ incorporates the interaction between the adlayer and the substrate[24,30].

Now, from Eq. (A1), the dimensional spatio-temporal evolution equations can be derived as

$$\frac{\partial \hat{\rho}_i}{\partial \hat{t}} = \hat{M}_\rho \hat{\nabla}^2 \left(\frac{\delta F_i}{\delta \hat{\rho}_i} \right) + \zeta_i^\rho, \tag{A2}$$

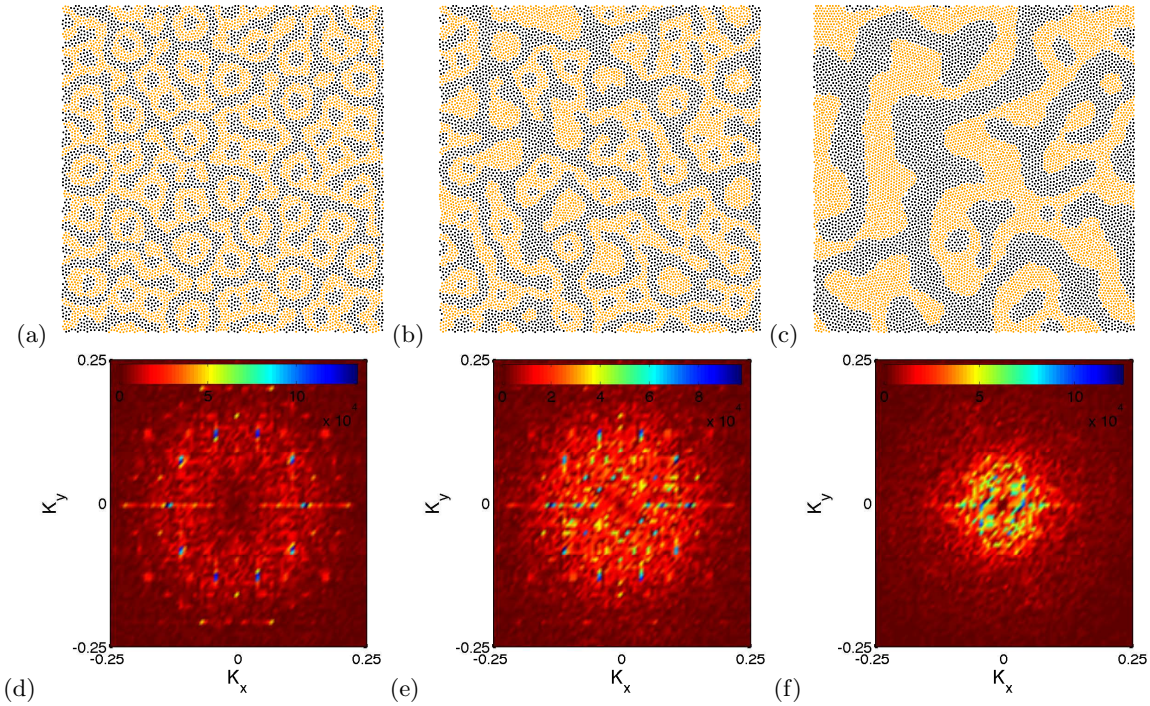

FIG. 7. (Color online) Compositional domain formation on quasicrystalline substrate at several line tension values: (a) $f_0 = 1.53 \times 10^{-2}$, (b) $f_0 = 2.45 \times 10^{-2}$, and (c) $f_0 = 4.29 \times 10^{-2}$. The corresponding compositional structure factors are shown in (d), (e), and (f), respectively. In all three cases, formation of strain-stabilized compositional domains is observed, with larger values of the line tension corresponding to larger domains, as expected. It can also be seen that at low line tensions, the structure factors show well-defined peaks that are ten-fold symmetric, reflecting the formation of compositional domains with QC symmetry. At larger line tension values, the domain structure begins to resemble the classical spinodal microstructure, which is reflected in the structure factor by virtue of the ten-fold symmetric peaks coalescing into a "ring" at the characteristic wavenumber of the spinodal microstructure.

and

$$\frac{\partial c_i}{\partial \hat{t}} = \hat{M}_c \hat{\nabla}^2 \left(\frac{\delta F_i}{\delta c_i} \right) + \zeta_i^c. \tag{A3}$$

Here, $\zeta_i^{\rho/c}$ denotes a Gaussian noise term with mean $\langle \zeta_i^{\rho/c} \rangle = 0$ and variance $\langle \zeta_i^{\rho/c}(\mathbf{r},t)\zeta_i^{\rho/c}(\mathbf{r}',t') \rangle = -2\hat{M}_{\rho/c}k_B T \hat{\nabla}^2 \delta(\hat{\mathbf{r}} - \hat{\mathbf{r}}')\delta(\hat{t} - \hat{t}')$ in accordance with the fluctuation-dissipation theorem. Introducing the non-dimensional variables

$$\mathbf{r} = q_{sub}\hat{\mathbf{r}}, \quad q_i(c) = \frac{\hat{q}_i(c)}{q_{sub}}, \quad \rho_i = \hat{\rho}_i \sqrt{\frac{u}{\lambda q_{sub}^4}}, \quad r = \frac{\hat{r}}{\lambda q_{sub}^4}, \quad t = \hat{M}_\rho \lambda q_{sub}^6 \hat{t} \tag{A4}$$
$$f_0 = \frac{u\hat{w}_0^2 \hat{f}_0}{\lambda^2 q_{sub}^6 w_0^2}, \quad V_i(c_i) = \frac{\hat{V}_i(c_i)u^{1/2}}{q_{sub}^6 \lambda^{3/2}}, \quad F = \frac{u\hat{F}}{q_{sub}^6 \lambda^2}, \quad \theta_{(c)} = \frac{k_B T_{(c)} w_0^2}{u q_{sub}^2 \hat{w}_0^2},$$

where q_{sub} denotes the substrate wave number, results in the non-dimensional free energy [Eq. (1) in the main text]

$$F_i[\rho_i, c_i] = \int \left[\left(\frac{\rho_i}{2} \left(r_i(c_i) + \left(q_i(c_i)^2 + \nabla^2 \right)^2 \right) \rho_i + \frac{\rho_i^4}{4} \right) + V_i(c_i)\rho_i + f_0 \left(\frac{w_0^2}{2} (\nabla c_i)^2 \right.\right.$$
$$\left.\left. - \frac{\theta_c}{2} c_i^2 + \frac{\theta}{2} [(1+c_i)\log(1+c_i) + (1-c_i)\log(1-c_i)] \right) \right] d\mathbf{r}, \tag{A5}$$

and the dimensionless dynamic equations [Eqs. (2) and (3) in the main text]

$$\frac{\partial \rho_i}{\partial t} = \nabla^2 \left(\frac{\delta F_i}{\delta \rho_i} \right) + \eta_i^\rho \tag{A6}$$

and

$$\frac{\partial c_i}{\partial t} = M_c \nabla^2 \left(\frac{\delta F_i}{\delta c_i} \right) + \eta_i^c, \tag{A7}$$

where $M_c \equiv (\hat{M}_c \lambda q_{sub}^4)/(\hat{M}_\rho u)$, and $\langle \eta_i^{c/\rho}(\mathbf{r},t)\eta_i^{c/\rho}(\mathbf{r}',t')\rangle = -2(\hat{M}_{c/\rho}/\hat{M}_\rho)\tilde{T}\nabla^2\delta(\mathbf{r}-\mathbf{r}')\delta(t-t')$. Finally, the dimensionless temperature is given by

$$\tilde{T} \equiv u k_B T/(q_{sub}^2 \lambda^2). \tag{A8}$$

Appendix B: Numerical method

1. Single component systems

In the case of single component systems, we employ the semi-implicit Fourier spectral method introduced by Cheng and Warren[52] for the spatio-temporal evolution of $\rho(\mathbf{r},t)$. With this method, ρ is integrated in time via

$$\tilde{\rho}_{n+1}^{\mathbf{k}} = \tilde{\rho}_n^{\mathbf{k}} - |\mathbf{k}|^2 \Delta t_{eff}^{PFC}(\mathbf{k},\Delta t)\{L_\rho^{\mathbf{k}} \tilde{\rho}_n^{\mathbf{k}} + \tilde{N}^{\mathbf{k}}[\rho_n]\} + \tilde{\eta'}^{\mathbf{k}}, \tag{B1}$$

where $\rho^{\mathbf{k}}$ denotes the fourier transform of ρ, Δt denotes the time step, the subscript n indicates the current time step,

$$\Delta t_{eff}^{PFC}(\mathbf{k},\Delta t) = \frac{\Delta t}{1 + \Delta t[(r+q_0^4)(1-a_1) + 2|\mathbf{k}|^2 q_0^2(a_2-1) + |\mathbf{k}|^4(1-a_3)]}; \tag{B2}$$

$$L_\rho^{\mathbf{k}} = (r + (q_0^2 - |\mathbf{k}|^2)^2); \quad \text{when } (r + (q_0^2 - |\mathbf{k}|^2)^2) < 12.5;$$
$$L_\rho^{\mathbf{k}} = 12.5; \quad \text{when } (r + (q_0^2 - |\mathbf{k}|^2)^2) > 12.5; \tag{B3}$$

and

$$N[\rho] = \rho^3 + V. \tag{B4}$$

Within this scheme, the parameters a_1, a_2, and a_3 are employed to optimize (i.e., maximize) the time step in the simulations resulting in numerically stable solutions. The noise function η was constructed using the method described in Petschek and Metiu[53], which is reiterated here for convinience. We know that

$$\langle \eta'(\mathbf{r}_1,t_1)\eta'(\mathbf{r}_2,t_2)\rangle = -2\tilde{T}\Delta t \nabla^2 \delta(\mathbf{r}_2 - \mathbf{r}_1). \tag{B5}$$

where,

$$\eta'(\mathbf{r},t) = \int_t^{t+\Delta t} \eta(\mathbf{r},t_1) dt_1. \tag{B6}$$

Within this formulation, η', which is the conserved noise, is constructed from two statistically independent Gaussian fields μ_1 and μ_2 as follows:

$$\eta'(x,y,t) = \left(\frac{\mu_1(x+\Delta x,y,t) - \mu_1(x,y,t)}{\Delta x} + \frac{\mu_2(x,y+\Delta y,t) - \mu_2(x,y,t)}{\Delta y} \right) \tag{B7}$$

where,

$$\langle \mu_1(\mathbf{r}_1,t_1)\mu_1(\mathbf{r}_2,t_2)\rangle = \langle \mu_2(\mathbf{r}_1,t_1)\mu_2(\mathbf{r}_2,t_2)\rangle = \frac{2\tilde{T}\Delta t}{\Delta x \Delta y} \tag{B8}$$

for $\mathbf{r}_1 = \mathbf{r}_2$ and $t_1 = t_2$ and

$$\langle \mu_1(\mathbf{r}_1,t_1)\mu_1(\mathbf{r}_2,t_2)\rangle = \langle \mu_2(\mathbf{r}_1,t_1)\mu_2(\mathbf{r}_2,t_2)\rangle = 0 \tag{B9}$$

otherwise. Furthermore, we introduce a cut-off wave number $k_{cut} = 2$, such that $\tilde{\eta'}^{\mathbf{k}} = 0$ for $|\mathbf{k}| > k_{cut}$.

2. Binary systems

In the case of binary systems, we employ the semi-implicit Fourier spectral method introduced by Zhu *et al.*[54] for the evolution of $c(\mathbf{r},t)$ and the semi-implicit Fourier spectral method discussed above for ρ. More specifically, the time-stepping algorithm used for the evolution of ρ is now given by

$$\tilde{\rho}^{\mathbf{k}}_{n+1} = \tilde{\rho}^{\mathbf{k}}_{n} - |\mathbf{k}|^2 \Delta t^{PFC}_{eff}(\mathbf{k},\Delta t)\{L^{\mathbf{k}}_{\rho}\tilde{\rho}^{\mathbf{k}}_{n} + \tilde{N}^{\mathbf{k}}[\rho_n]\}, \tag{B10}$$

where,

$$\Delta t^{PFC}_{eff}(\mathbf{k},\Delta t) = \frac{\Delta t}{1+\Delta t[(r+1)(1-a_1)+2|\mathbf{k}|^2(a_2-1)+|\mathbf{k}|^4(1-a_3)]}; \tag{B11}$$

$$L^{\mathbf{k}}_{\rho} = (r+(1-|\mathbf{k}|^2)^2); \quad \text{when } (r+(1-|\mathbf{k}|^2)^2) < 12.5;$$
$$L^{\mathbf{k}}_{\rho} = 12.5; \quad \text{when } (r+(1-|\mathbf{k}|^2)^2) > 12.5; \tag{B12}$$

and

$$\begin{aligned} N[\rho] = &\left(\rho^3 + \frac{r(+1)-r(-1)}{2}\rho c + V_i(c)\right) \\ &+\epsilon\Big(-2c\rho - 2c\nabla^2\rho - 2\nabla\rho\cdot\nabla c - \rho\nabla^2 c\Big) \\ &+\epsilon^2\left(\frac{5}{2}\rho c^2 + \frac{3}{2}c^2\nabla^2\rho + 3c\nabla\rho\cdot\nabla c + \frac{3}{2}\rho|\nabla c|^2 + \frac{3}{2}\rho c\nabla^2 c\right). \end{aligned} \tag{B13}$$

The time-stepping algorithm used for the evolution of c is given by:

$$\tilde{c}^{\mathbf{k}}_{n+1} = \frac{4\tilde{c}^{\mathbf{k}}_{n} - \tilde{c}^{\mathbf{k}}_{n-1} - |\mathbf{k}|^2\big(2\tilde{N}^{\mathbf{k}}[c_n] - \tilde{N}^{\mathbf{k}}[c_{n-1}]\big)2M_c\Delta t}{(3-2M_c\Delta t L^{\mathbf{k}}_{c})}; \tag{B14}$$

$$L^{\mathbf{k}}_{c} = -f_0 w_0^2 |\mathbf{k}|^2; \tag{B15}$$

and

$$\begin{aligned} N[c] = &\left(f_0\left((-\theta_c+\theta)c + \theta\left(\frac{c^3}{3}+\frac{c^5}{5}+\cdots\frac{c^{51}}{51}\right)\right) + \frac{r(+1)-r(-1)}{4}\rho^2 + \right. \\ &\left.\frac{V(+1)-V(-1)}{2}\rho\right) - \epsilon\left(\rho^2 + \rho\nabla^2\rho\right) + \epsilon^2\left(\frac{5}{2}\rho^2 c + \frac{3}{2}\rho c\nabla^2\rho\right). \end{aligned} \tag{B16}$$

Finally, the spatial derivatives of the variables in Eqs. (B13) and (B16) are computed up to fourth order accuracy in Δx and Δy. In particular, first order spatial derivatives are computed using

$$\begin{aligned} \frac{\partial g}{\partial x} = \frac{1}{\Delta x}\Big(&-\frac{1}{12}g(x+2\Delta x,y,t) + \frac{2}{3}g(x+\Delta x,y,t) - \frac{2}{3}g(x-\Delta x,y,t) \\ &+\frac{1}{12}g(x-2\Delta x,y,t)\Big) \end{aligned} \tag{B17}$$

$$\begin{aligned} \frac{\partial g}{\partial y} = \frac{1}{\Delta y}\Big(&-\frac{1}{12}g(x,y+2\Delta y,t) + \frac{2}{3}g(x,y+\Delta y,t) - \frac{2}{3}g(x,y-\Delta y,t) \\ &+\frac{1}{12}g(x,y-2\Delta y,t)\Big), \end{aligned} \tag{B18}$$

while the Laplacian is evaluated using

$$\begin{aligned} \nabla^2 g = &\frac{1}{\Delta x^2}\Big(-\frac{1}{12}g(x+2\Delta x,y,t) + \frac{4}{3}g(x+\Delta x,y,t) + \frac{4}{3}g(x-\Delta x,y,t) \\ &-\frac{1}{12}g(x-2\Delta x,y,t) - \frac{5}{2}g(x,y,t)\Big) + \frac{1}{\Delta y^2}\Big(-\frac{1}{12}g(x,y+2\Delta y,t) + \\ &\frac{4}{3}g(x,y+\Delta y,t) + \frac{4}{3}g(x,y-\Delta y,t) + \frac{1}{12}g(x,y-2\Delta y,t) - \frac{5}{2}g(x,y,t)\Big). \end{aligned} \tag{B19}$$

* smuralid@princeton.edu
† mhaataja@princeton.edu

[1] M. Haruta, Catalysis Today **36**, 153 (1997).
[2] A. W. Stephenson, C. J. Baddeley, M. S. Tikhov and R. M. Lambert, Surf. Sci. **398**, 172 (1998).
[3] J. Bansmann *et al.*, Surf. Sci. Rep. **56**, 189 (2005).
[4] A. N. Grigorenko, N. W. Roberts, M. R. Dickinson and Y. Zhang, Nature **2**, 365 (2008).
[5] J. V. Barth, G. Costantini, and K. Kern, Nature, **437**, 671 (2005).
[6] H. Brune, M. Giovannini, K. Bromann, K. Kern, Nature, **394**, 451 (1998).
[7] S. Rousset, B. Croset, Y. Girard, G. Prevot, V. Repain, and S. Rohart, C. R. Physique **6**, 33 (2005).
[8] F. C. Frank and J. H. van der Merwe, Proc. Roy. Soc. London A **198**, 205 (1949).
[9] P. Bak, Rep. Prog. Phys. **45**, 587 (1982).
[10] J . C. Hamilton and S. M. Foiles, Phys. Rev. Lett. **75**, 882 (1995).
[11] R. Q. Hwang, J. C. Hamilton, J. L. Stevens, and S. M. Foiles, Phys. Rev. Lett. **75**, 4242 (1995).
[12] W. L. Ling *et al.*, Surf. Sci. **600**, 1735 (2006).
[13] W. G. Cullen and P. N. Frist, Surf. Sci. **420**, 1 (1999).
[14] R. McGrath, J. Ledieu, E. J. Cox, and R. D. Diehl, J. Phys. Condens. Matter **14**, R119 (2002).
[15] R. McGrath, J. Ledieu, E. J. Cox, N. Ferralis, and R. D. Diehl, J. Non-Cryst. Solids **334-335**, 500 (2004).
[16] V. Fournee and P. A. Thiel, J. Phys. D: Appl. Phys. **38**, R83 (2005).
[17] J. A. Smerdon, H. R. Sharma, J. Ledieu, and R. McGrath, J. Phys. Condens. Matter **20**, 314005 (2008).
[18] B. Unal *et al.* Phys. Rev. B **75**, 064205 (2007).
[19] T. Cai, J. Ledieu, R. McGrath, V. Fourne, T. Lograsso, A. Ross, P. Thiel, Surface Science, **526**, 115-120 (2003).
[20] I. Daruka and J. C. Hamilton, J. Phys.: Condens. Matter **15**, 1827 (2003).
[21] V. Ozolins, M. Asta, and J. J. Hoyt, Phys. Rev. Lett. **88**, 096101 (2002).
[22] B. Yang, T. Muppidi, V. Ozolins, and M. Asta, Phys. Rev. B **77**, 205408 (2008).
[23] B. Yang, T. Muppidi, V. Ozolins, and M. Asta, Surf. Sci. **602**, L123 (2008).
[24] S. Muralidharan and M. Haataja, Phys. Rev. Lett. **105**, 126101 (2010).
[25] K. Elder, M. Katakowski, M. Haataja, and M. Grant, Phys. Rev. Lett. **88**, 245701 (2002).
[26] K. R. Elder and M. Grant, Phys. Rev. E. **70**, 051605, (2004).
[27] P. Stefanovic, M. Haataja, and N. Provatas, Phys. Rev. Lett. **96**, 225504 (2006).
[28] K. R. Elder, N. Provatas, J. Berry, P. Stefanovic, and M. Grant, Phys. Rev. B **75**, 064107, (2007).
[29] K. R. Elder, Z. F. Huang and N. Provatas, Phys. Rev. E **81**, 011602, (2010).
[30] C. V. Achim *et al.*, Phys. Rev. E **74**, 021104, (2006).
[31] Z.-F. Huang and K. R. Elder, Phys. Rev. Lett. **101**, 158701 (2008).
[32] K.-A. Wu and P. W. Voorhees, Phys. Rev. B **80**, 125408, (2009).
[33] G. Tegze, G. I. Tóth, and L. Gránásy, Phys. Rev. Lett. **106**, 195502 (2011).
[34] J. Rottler, M. Greenwood, and B. Ziebarth, J. Phys.: Cond. Matter **24**, 135002 (2012).
[35] J. Ledieu, M. Krajčí, J. Hafner, L. Leung, L. H. Wearing, R. McGrath, T. A. Lograsso, D. Wu, and V. Fournée, Phys. Rev. B **79**, 165430 (2009).
[36] K. R. Elder, M. Grant, N. Provatas, and J. M. Kosterlitz, Phys. Rev. E **64**, 021604 (2001).
[37] L. Q. Chen, Annu. Rev. Mat. Res. **32**, 113 (2002).
[38] W. J. Boettinger, J. A. Warren, C. Beckermann, and A. Karma, Annu. Rev. Mat. Res. **32**, 163 (2002).
[39] M. Haataja, L. Gránásy, and H. Löwen, J. Phys.: Cond. Matter **22**, 360301 (2010).
[40] J. H. Van der Merwe, Interf. Sci. **1**, 77 (1993).
[41] O. L. Alerhand, D. Vanderbilt, R. D. Meade, and J. D. Joannopoulos, Phys. Rev. Lett. **61**, 1973 (1988).
[42] K.-O. Ng and D. Vanderbilt, Phys. Rev. B **52**, 2177 (1995).
[43] V. Shchukin and D. Bimberg, Rev. Mod. Phys. **71**, 1125 (1999).
[44] J. W. Matthews and A. E. Blakeslee, J. Cryst. Growth **27**, 118 (1974).
[45] H. Gao and W. D. Nix, Annu. Rev. Mater. Sci **29**, 173 (1999).
[46] A possible exception is provided by certain domain "cleavage" processes discussed in Sec. III A 3). However, even in this case, we verify that the effect of thermal fluctuations in the concentration field can be neglected within a reasonable range of temperature values.
[47] S. Narasimhan and D. Vanderbilt, Phys. Rev. Lett. **69**, 1564 (1992).
[48] K. Thürmer, C. B. Carter, N. C. Bartelt and R. Q. Hwang, Phys. Rev. Lett. **10**, 106101 (2004).
[49] L Gránásy, G. Tegze, G. I. Tóth, and T. Pusztai, Phil. Mag. **91**, 123 (2011).
[50] J. Mikhael, J. Roth, L. Helden, and C. Bechinger, Nature **454**, 501 (2008).
[51] S. P. Gorkhali, J. Qi, and G. P. Crawford, Appl. Phys. Lett. **86**, 011110 (2005).
[52] M. Cheng and J. A. Warren, J. Comput. Phys. **227**, 6241 (2008).
[53] R. G. Petschek and H. Metiu, J. Chem. Phys. **79**, 3443 (1983).
[54] J. Z. Zhu, L. Q. Chen, J. Shen, and V. Tikare, Phys. Rev. E. **60**, 3564 (1999).